ADVANCED ELECTRONIC MATERIALS
www.advelectronicmat.de

Semiconductor-to-Metal Transition and Quasiparticle Renormalization in Doped Graphene Nanoribbons

Boris V. Senkovskiy, Alexander V. Fedorov, Danny Haberer, Mani Farjam, Konstantin A. Simonov, Alexei B. Preobrajenski, Niels Mårtensson, Nicolae Atodiresei, Vasile Caciuc, Stefan Blügel, Achim Rosch, Nikolay I. Verbitskiy, Martin Hell, Daniil V. Evtushinsky, Raphael German, Tomas Marangoni, Paul H. M. van Loosdrecht, Felix R. Fischer,* and Alexander Grüneis**

A semiconductor-to-metal transition in $N = 7$ armchair graphene nanoribbons causes drastic changes in its electron and phonon system. By using angle-resolved photoemission spectroscopy of lithium-doped graphene nanoribbons, a quasiparticle band gap renormalization from 2.4 to 2.1 eV is observed. Reaching high doping levels (0.05 electrons per atom), it is found that the effective mass of the conduction band carriers increases to a value equal to the free electron mass. This giant increase in the effective mass by doping is a means to enhance the density of states at the Fermi level which can have palpable impact on the transport and optical properties. Electron doping also reduces the Raman intensity by one order of magnitude, and results in relatively small (4 cm^{-1}) hardening of the G phonon and softening of the D phonon. This suggests the importance of both lattice expansion and dynamic effects. The present work highlights that doping of a semiconducting 1D system is strikingly different from its 2D or 3D counterparts and introduces doped graphene nanoribbons as a new tunable quantum material with high potential for basic research and applications.

Graphene nanoribbons (GNRs) are promising materials for the production of nanoscale devices.[1–5] In contrast to graphene, GNRs can be metallic or semiconducting with a tunable band gap that depends on the ribbon width and the edge configuration.[6–10] Carbon nanotubes are a similar 1D material but despite a 20 year history, the large-area synthesis of monochiral carbon nanotubes remains challenging.[11] On the other hand, nanoribbons can be fabricated with atomically controlled precision thanks to the bottom-up nanofabrication techniques.[12–20] Thus, GNRs combine the best attributes of the nanotube and graphene worlds.

Engineering of GNR-based optoelectronic devices requires an understanding of the charge transfer effect on the

Dr. B. V. Senkovskiy, Dr. A. V. Fedorov, Dr. N. I. Verbitskiy, M. Hell, R. German, Prof. P. H. M. van Loosdrecht, Prof. A. Grüneis
II. Physikalisches Institut
Universität zu Köln
Zülpicher Strasse 77, Köln 50937, Germany
E-mail: senkovskiy@ph2.uni-koeln.de; grueneis@ph2.uni-koeln.de

Dr. A. V. Fedorov
St. Petersburg State University
Ulyanovskaya ul. 1, St. Petersburg 198504, Russia

Dr. A. V. Fedorov
IFW-Dresden
Dresden
Helmholtzstraße 20, 01069, Germany

Dr. D. Haberer, Dr. T. Marangoni, Prof. F. R. Fischer
University of California at Berkeley
699, Tan Hall, Berkeley, CA 94720, USA
E-mail: ffisher@berkeley.edu

Dr. M. Farjam
School of Nano Science
Institute for Research in Fundamental Sciences (IPM)
P.O. Box 19395-5531, Tehran, Iran

Dr. K. A. Simonov, Prof. N. Mårtensson
Department of Physics and Astronomy
Uppsala University
Box 516, Uppsala 75120, Sweden

Dr. K. A. Simonov, Dr. A. B. Preobrajenski
MAX IV
Lund University
Box 118, Lund 22100, Sweden

Dr. N. Atodiresei, Dr. V. Caciuc, Prof. S. Blügel
Peter Grünberg Institut (PGI-1) and Institute for Advanced Simulation (IAS-1)
Forschungszentrum Jülich and JARA
Jülich D-52425, Germany

Prof. A. Rosch
Institute for Theoretical Physics
Universität zu Köln
Zülpicher Strasse 77, Köln 50937, Germany

Dr. N. I. Verbitskiy
Faculty of Physics
University of Vienna
Strudlhofgasse 4, Vienna A-1090, Austria

Dr. N. I. Verbitskiy
Department of Materials Science
Moscow State University
Leninskiye Gory 1/3, Moscow 119992, Russia

Dr. D. V. Evtushinsky
Helmholtz-Zentrum Berlin für Materialien und Energie
Elektronenspeicherring BESSY II
Albert-Einstein-Strasse 15, Berlin 12489, Germany

DOI: 10.1002/aelm.201600490

electronic and optical properties of GNRs. This effect could be large taking into account the importance of many-body physics for low-dimensional materials. For example, charge transfer induced many-body interactions have been theoretically predicted for semiconducting quantum wells,[21] carbon nanotubes,[22] and 2D layers.[23] The inclusion of electron–electron interactions in GNRs in the framework of the "GW" approximation leads to a larger QP band gap,[7,24,25] which can be significantly reduced by screening from a metallic substrate.[26] Similarly, as the charge carrier density is increased, one might expect stronger screening of the Coulomb interactions and as a consequence a smaller band gap. Thus, charge doping of GNRs could be an efficient tool to manipulate many-body interaction and to control their optical and electronic properties. Indeed, for carbon nanotubes there is experimental evidence for a band gap renormalization upon charge doping.[27–30] Moreover, it has been put forward by theory that the dynamical screening due to acoustic charge carrier plasmons, which have a unique contribution in a 1D system, also leads to the effective mass renormalization in semiconducting nanotubes upon a transition to the metallic state.[22] The band gap and the charge-carrier effective mass determine the optical, electronic, and thermal properties of the material. However, the full picture of the quasiparticle (QP) renormalization in a 1D material caused by charge doping has not been experimentally proven.

To shed light on this issue we perform electron doping of aligned $N = 7$ armchair graphene nanoribbons (7-AGNRs) using lithium atoms as a charge donor. A multitechnique approach is a key that allows us to gather a complete picture of the physical properties of doped GNRs. First, we apply angle-resolved photoemission spectroscopy (ARPES) to directly observe the renormalization of their electronic band structure upon doping. Second, by X-ray photoemission spectroscopy (XPS) and near edge X-ray absorption fine structure (NEXAFS) spectroscopy we show that lithium does not distort the ribbon's structure and that the antibonding π^* states are filled with electrons. Then, the experimental data are compared against density functional theory (DFT) calculations of the electron energy band structure without explicit inclusion of many-body interactions. Finally, we apply ultrahigh vacuum (UHV) Raman spectroscopy and show a transition from resonance to off-resonance Raman and phonon energy renormalization in Li-doped GNRs.

The unprecedented structural quality of massively parallel 7-AGNRs uniformly aligned on the vicinal surface of Au(788) single crystal and their flatness opens up the use of powerful spectroscopic methods such as ARPES.[26,31] **Figure 1** shows the second derivative of the ARPES intensity maps (raw data are shown in the Supporting Information) measured in the direction parallel to the axis of the 7-AGNRs. The second derivative method is used to enhance the band features. Three parabola-like electronic valence sub-bands of pristine 7-AGNRs can be clearly seen in Figure 1a. Using parabolic fits of the raw ARPES data at the band maxima we determined the position of the valence band maximum (VBM) $E_{V1} = 0.88$ eV and the effective mass at the VBM $m^*_{V1} = -0.23\ m_e$ (here m_e indicates the free electron mass and V_1 is the first valence sub-band). Our value for m^*_{V1} is in good agreement to the work of ref. [26] ($-0.21\ m_e$). The values of the energies E_{V2} and E_{V3} and corresponding effective masses m^*_{V2} and m^*_{V3} are given in the caption of Figure 1.

Figure 1b shows that after in situ deposition of one monolayer (ML) of Li the valence band shifts down by 1.33 ± 0.05 eV and higher photoemission intensity appears at the Fermi level. This feature is assigned to the conduction band of Li-doped 7-AGNRs. The energy separation between valence and conduction bands was found to be about 2.1 eV. Interestingly, this value is significantly lower than the band gaps measured by STS for 7-AGNRs on Au(111): 2.7,[32] 2.3,[26] 2.5,[14] and 2.37 eV.[33] Our scanning tunneling spectroscopy (STS) data, shown in the Supporting Information, provide the same band gap for 7-AGNRs on Au(788) and on Au(111): 2.4 eV, which is in a good agreement with the previous works. It is important to point out that a precise STS measurement of Li-doped nanoribbons is hampered by the prohibitively high Li mobility. The difference between the band gaps obtained by ARPES and STS is equal to the self-energy corrections due to charge transfer doping and can directly be compared to the theoretical predictions. Our analysis relies on the fact that STS and ARPES reveal identical energy band dispersions which has been explicitly shown for GNRs.[34] A similar approach of comparing STS derived QP band gap and the optical gap of $MoSe_2$ monolayers

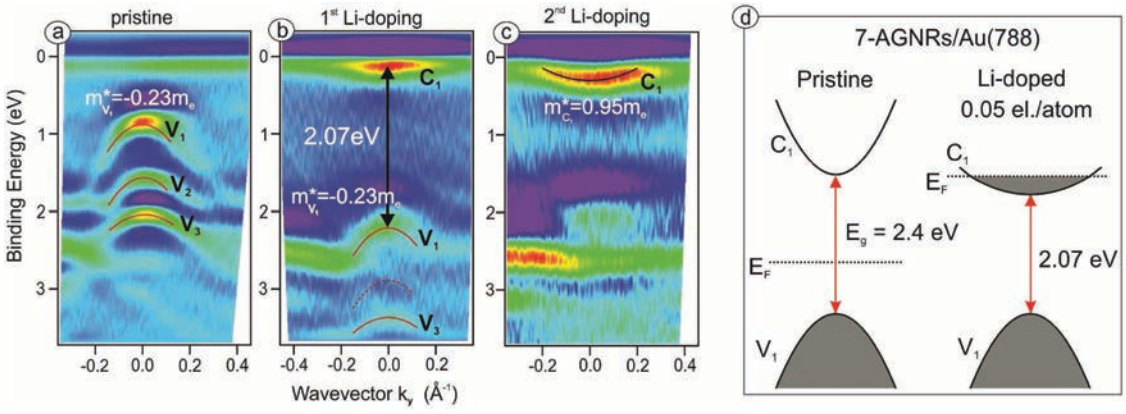

Figure 1. ARPES data (second derivative) of aligned 7-AGNRs on Au(788) accumulated along the k_y direction with respect to the second Brillouin zone. a) Pristine 7-AGNRs. The maximum energies (effective masses) of V_1, V_2, and V_3 sub-bands are 0.88 eV ($-0.23\ m_e$), 1.56 eV ($-0.23\ m_e$), and 2.04 eV ($-0.41\ m_e$), respectively. b) After first Li-doping (about 1 ML). The dashed parabola indicates where the V_2 sub-band should be (it is not visible due to the overlap with Au 5d states). c) After second Li-doping (about 2 ML). d) Illustration of the observed electronic band renormalization in Li-doped 7-AGNRs.

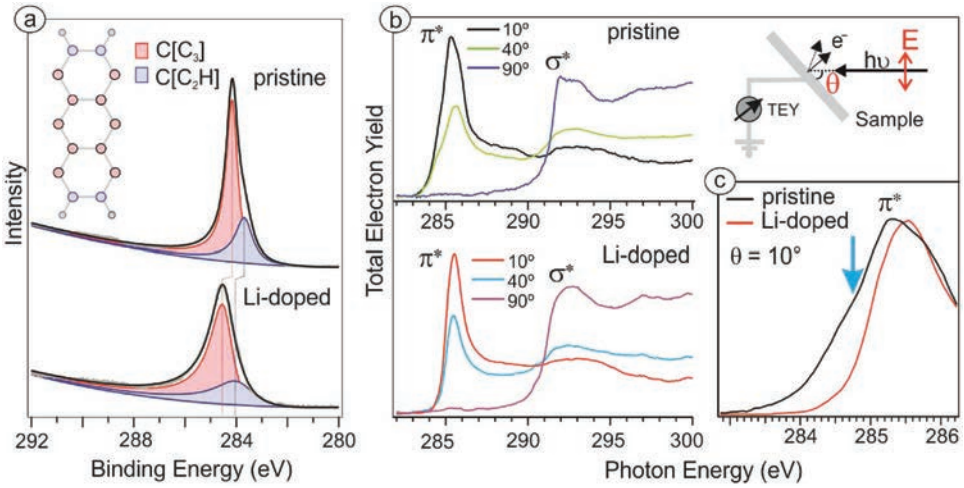

Figure 2. a) XPS spectra of the C1s core level of 7-AGNRs/Au(788) before and after deposition of 1 ML of Li, measured with 320 eV photon energy. b) Angle-dependent NEXAFS spectra of 7-AGNRs/Au(788) at the C K-edge probed by linearly polarized radiation before and after Li doping. A sketch of the experimental geometry is depicted in the inset. c) Close-up of the π^* resonance at grazing angle. The blue arrow indicates the disappearance of the low-energy shoulder after Li-doping.

has yielded the exciton binding energies directly.[35] Thus, Li doping reduces the QP band gap by ≈300 meV.

In order to have a higher doping to reliably fit the effective mass of the conduction band, we have performed a second deposition of Li. Figure 1c shows the corresponding spectrum which clearly exhibits a parabola-like feature. This is the maximum doping level we achieved and the area of the 1D Brillouin zone (BZ), occupied by the conduction band below the Fermi level, suggests that the doping level is about 1.7 ± 0.1 electrons nm^{-1} or 0.05 electrons per carbon atom. The parabola-like dispersion of the conduction sub-band C_1 has a strikingly large value of the effective mass of 0.95 ± 0.05 m_e. From zone-folding we expect approximate electron–hole symmetry in the electronic structure of 7-AGNRs. Therefore, the absolute values of the effective masses of valence and conduction bands should be close to one another. This is also consistent with DFT results[6,36,37] for undoped ribbons and with STS data.[33] Recently, by means of Fourier transformed STS, the effective electron masses of V_1 and C_1 were also estimated for isolated 7-AGNRs on NaCl as 0.32 and 0.35 m_e, correspondingly.[38] The value of the electron mass for the unoccupied conduction band is thus just slightly larger than the mass for the valence band. The experimentally observed mass renormalization approximately by a factor of four induced by electron doping is thus related to the strong electronic correlations that are present in 1D systems.[22,29] Our observations regarding the electronic band renormalization in GNRs induced by Li doping are summarized in Figure 1d.

The observed QP renormalization in doped GNRs demands additional experimental confirmation. First, one has to be sure that the structure of GNRs does not suffer by chemical functionalization and we have the same material before and after the Li deposition. Second, the filling of the conduction band has to be proved.

We performed XPS studies of the C1s core level to analyze the chemical composition of Li-doped 7-AGNRs. **Figure 2**a depicts the C1s spectra of 7-AGNRs before and after Li doping. Here, the $C[C_3]$ component belongs to the carbon atoms having three neighboring carbons and $C[C_2H]$ denotes the edge carbons with two carbon bonds and one hydrogen bond.[39] After Li deposition, both components shift to higher binding energies by the same amount due to charge transfer. The intensity ratio of the two components before and after the doping is 5:2 as expected from the structure. This indicates a structural quality with no or very few missing hydrogen atoms along the edges.

To investigate possible corrugations of the 7-AGNRs as a result of Li adsorption we performed a NEXAFS spectroscopy study of pristine and doped samples. Moreover, NEXAFS measurements are sensitive to the occupation of the conduction band. The series of C K-edge absorption spectra of 7-AGNRs are shown in Figure 2b. The angle-dependent behavior of the π^* and σ^* resonances suggests a planar structure of ribbons before and after Li deposition. Figure 2c shows a zoom of the π^* region of the NEXAFS spectrum. The low-energy shoulder of the π^* resonance is clearly visible in the NEXAFS spectrum of pristine GNRs. However, after Li deposition it disappears. This is because the transition from the C1s core level to the lowest conduction band states is blocked after electron doping. Due to the element-specific nature of the NEXAFS method, this gives a proof of the occupation of the carbon derived π^* levels.

Here, by means of DFT, we investigate the impact of charge transfer and the presence of Li ions on the electronic band structure of 7-AGNRs. The calculations do not include many-body effects (such us electron–plasmon and electron–electron Coulomb interactions). **Figure 3** depicts the DFT calculated 1D electron energy bands of pristine and Li-doped 7-AGNRs in the ground-state geometries together with the related structure configurations.

The configuration we consider in Figure 3b is one where the Li is placed above the center benzene ring of an anthracene unit. The second configuration shown in Figure 3c is one where two Li atoms are placed above the edge benzene rings

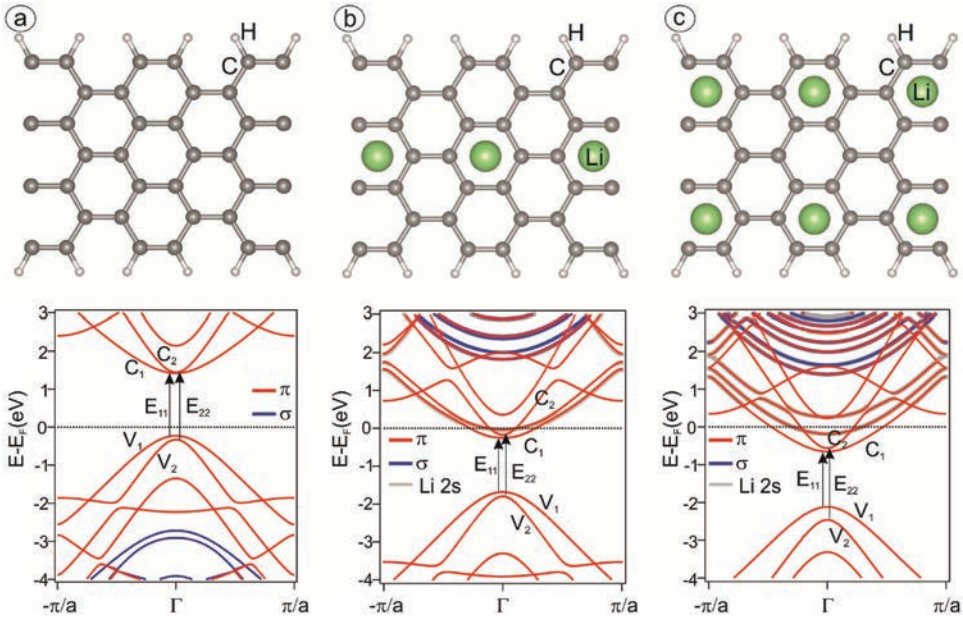

Figure 3. Electronic energy band structure and atomic structure of a) pristine and the ground state for b) one Li- and c) two Li-doped 7-AGNRs. The labels V_1 (V_2) and C_1 (C_2) depict the first (second) valence and conduction sub-bands, respectively. The red (blue) color indicates a π (σ) character of the respective band, the electronic bands with Li character are marked with gray. First and second transition energies between symmetric sub-bands with respect to the Fermi level E_F are labeled as E_{11} and E_{22}.

of the anthracene unit. In the Supporting Information we also show other possible configurations.

The interaction of Li with the 7-AGNR leads to a complete electron transfer from Li to the nanoribbon. The experimentally observed doping level suggests that there are about 0.7 electrons per unit cell (one anthracene unit). Taking into account charge leakage to the metallic substrate commonly observed for graphene on metals,[40] we can assume that the configuration with one Li atom per 7-AGNR unit cell is the most relevant to our experimental data. Moreover, Li atoms should be placed in the center with respect to long edges of the ribbon, otherwise the minimum of the conduction band is not located at the Γ-point of the BZ (see the Supporting Information), which is not observed in the experiment. The effective masses at the conduction band minima and valence band maxima for the configuration shown in Figure 3 are listed in **Table 1**. Let us compare the DFT results for the configurations with one Li atom in the center of the 7-AGNR unit cell (Figure 3b) to the ARPES data. Calculations show that the E_{11} and E_{22} transition energies follow opposite trends with doping: E_{11} decreases (by 0.19 eV) and E_{22} slightly increases (by 0.05 eV). Qualitatively, the ARPES data are in agreement with the DFT results in that the Li doping is reducing the VB-CB separation. DFT calculations demonstrate electron–hole asymmetry in the effective masses: m^*_{C1} is 34% larger than m_{V1}. This difference is increased by doping up to 55% in configuration with one Li atom. However, the experimentally observed difference is ≈400% which is not captured by the DFT model. This leads to the partial occupation of the second C_2 sub-band in the DFT calculations, while in experiment all transferred charge is accepted by the heavier C_1 sub-band.

Table 1. DFT results for pristine and Li-doped 7-AGNRs with different amount of Li atoms per unit cell for configurations shown in Figure 3: effective masses of the first valence (V_1) and conduction (C_1) sub-bands, energies of E_{11} and E_{22} transitions.

	Pristine	With one Li atom	With two Li atoms
m^*_{V1} [m_e][a)]	0.41	0.4	0.39
m^*_{C1} [m_e]	0.55	0.62	0.55
E_{11} [eV]	1.64	1.43	1.47
E_{22} [eV]	1.75	1.8	1.9

[a)] m_e is the free electron mass.

The experimentally observed large charge carrier mass can be attributed to many-body effects beyond the DFT approach. Indeed, the effective mass renormalization is determined by the energy and momentum dependence of the electron self-energy,[41] which include many-body interactions such as electron–phonon and electron–electron coupling. Alkali-metal doping of graphene induces large electron–phonon coupling, which manifests itself by kinks in the linear band dispersion.[42] In our case, the conduction band of doped GNRs is very shallow and does not allow us to make a statement regarding the degree of electron–phonon induced renormalization. Inclusion of the Coulomb interaction and its dynamical screening in the GW approach leads to an increase of the Fermi velocity in graphene[43] and smaller (10%) effective electron masses for undoped 7-AGNRs.[38] Thus, one can assume an increase of the effective mass due to the screened electron–electron interaction by the extra charge carriers in Li-doped system. Another contribution can be expected from the dynamical screening due to acoustic plasmons, which in theory can cause large effective mass renormalization in degenerately doped 1D semiconducting materials, as it was shown for carbon nanotubes.[22] Since the electronic structure of nanotubes and nanoribbons is very similar to each other (both are obtained by zone folding

of graphene), it is natural to expect that the quasiparticle renormalization of the band gap and effective mass due to the plasmon peaks in the loss function is leading to the same final result, that is, a reduced band gap and increased effective mass.

The semiconductor-to-metal transition should also affect the vibrational spectrum of 7-AGNRs. To investigate this effect we performed in situ Raman measurements of Li-doped GNRs in a specially built UHV Raman chamber. A commercially available Raman system was combined with an UHV setup where the GNR synthesis and Li doping have been performed as shown in a sketch in **Figure 4**a. The E_{22} optical transition energy for 7-AGNRs/Au(788) was experimentally found to be equal to 2.3 eV.[44] We have taken advantage of the large optical response at the van Hove singularities to perform resonance Raman spectroscopy measurements with a 532 nm (≈2.33 eV) laser. The UHV Raman spectra of 7-AGNRs on Au(111) and Au(788) before and after deposition of Li are shown in Figure 4b. The amount of deposited Li was close to the maximum doping level in ARPES (Figure 1c). After Li doping, a reduction in the Raman intensity by a factor of ≈20 is observed. The unique combination of UHV Raman and ARPES measurements on identical samples allows us to elucidate the reason of the observed Raman intensity loss. Looking to the ARPES spectrum of Figure 2b,c it is clear that the C_2 sub-band is not occupied and therefore the E_{22} transition is not blocked by the Pauli exclusion principle. Thus, there could be two reasons for the renormalization of the E_{22} optical transition energy. The first is a change in the QP band energies and the second is a reduction of the exciton binding energy. It was theoretically predicted that the dynamical screening effects induced in carbon nanotubes by a semiconductor-to-metal-transition substantially reduce the QP energy gap associated with the E_{22} transition; however, the decrease of the exciton binding energy is larger than the reduction of the QP gap making the effective optical gap larger.[22] Since the excitonic effect is intrinsically large for ultra-narrow graphene nanoribbon of only several carbon atoms width,[44] we expect a large renormalization of the optical transitions upon charge doping.

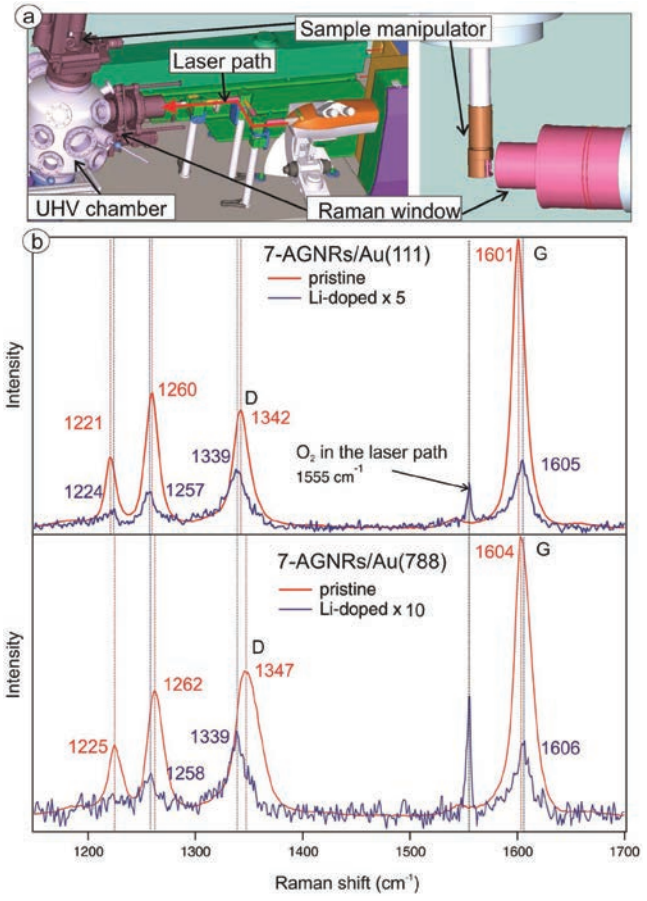

Figure 4. a) The UHV Raman system consists of a specially designed optical flange that connects a commercial Raman setup with an UHV system. The sample is mounted on a motorized manipulator. b) UHV Raman spectra of 7-AGNRs on Au(111) and on Au(788) measured before and after Li deposition with a 532 nm laser.

We note that the Raman modes of pristine ribbons on Au(788) are upshifted relative to the ribbons on Au(111) as a result of the higher density and hence larger inter-ribbon interaction (see STM data and assignment of the Raman modes in the Supporting Information). This situation is analogous to the upshift of the radial breathing mode in carbon nanotube bundles compared to isolated carbon nanotubes.[45] Li doping seems to decrease the inter-ribbon interaction and results in Raman peaks for ribbons on Au(111) and Au(788) substrates that are very close to one another. Thus, to discuss the doping-induced phonon energy renormalization it is better to consider the system on Au(111).

For 7-AGNRs on Au(111) we observe the energy upshift for the G peak ≈4 cm^{-1} after Li doping while the D peak and the peak at 1260 cm^{-1} are downshifted by 3 cm^{-1} (the intensity of the peak at 1221 cm^{-1} is too weak to make a statement regarding its shift). Graphene at doping levels of 5×10^{13} electrons cm^{-2} or 0.013 electrons/atom (≈4 times smaller than in our case) exhibits much larger upshift of the G mode by ≈20 cm^{-1}.[46,47] The reason is that graphene in its pristine state is a semimetal and the Kohn anomaly in the phonon dispersion at wavevector $q = \Gamma$ disappears with doping.[46] Unlike graphene, ribbons are intrinsically semiconductors and do not exhibit a Kohn anomaly prior to doping. Upon doping we expect that a Kohn anomaly appears at $q_y = 2k_F$ (where k_F is the Fermi wavevector). Since for GNRs the mass renormalization is so strong, the conduction band becomes flat and the Fermi wavevector k_F rapidly moves away from the apex of the conduction band parabola. This shifts the $q_y = 2k_F$ phonon away from the BZ center and the Kohn anomaly does not affect Γ point phonons.

The present experimental Raman data are best rationalized using a similar reasoning as for doped semiconducting nanotubes. In semiconducting carbon nanotubes the total change in the phonon frequency of the G mode was rationalized in terms of dynamic and static contributions[48]

$$\Delta\omega = \Delta\omega^{\text{static}} + \Delta\omega^{\text{dyn}} \quad (1)$$

The static term reflects the increase of the lattice constant resulting from the filling of antibonding states. This term is negative for electron doping and positive for hole doping.[48,49] The dynamic contribution is always positive and occurs as a result of the reduced screening of the lattice vibration by the

charge carriers. The dynamic effects describe changes beyond the adiabatic Born–Oppenheimer approximation.[48,50–52] It depends on the electronic structure of the sp^2 carbon material, the phonon branch, and wavevector, and the doping level on which these competing factors prevail. In electron-doped semiconducting carbon nanotubes these two contributions balance each other, resulting in only a slight upshift of the G mode.[48,52] Based on the structural similarity of nanotubes and nanoribbons we suppose the same for our system. In the Supporting Information we also estimated the Raman shift for the G mode of 7-AGNRs based on theory for graphene and nanotubes. A full quantitative agreement cannot be expected, since the C—C bond lengths in doped 7-AGNR are affected in an inhomogeneous manner. However, according to our DFT calculations the bond lengths of nanoribbons fall within less than 2% of the graphene bond length. We obtained that both contributions are the same order of magnitude and that the dynamic effects prevail. In regards to the downshift of the other phonon modes we ascribe this to the dominance of lattice expansion.

As a result of the relatively small phonon energy shifts upon electron doping (compared to graphene) we propose that for application of GNRs it is better not to use the Raman shifts but the intensity changes as an indicator of doping level. It can also be noted that one can expect much larger shift of the Raman modes of semiconducting GNRs for the hole doping as the dynamic and static terms have a positive sign. Thus, the electron/hole doping asymmetry in the Raman shifts for GNRs can be proposed to the future experimental studies.

In conclusion, we demonstrate that ultranarrow graphene nanoribbons are a new functional nanomaterial which can be effectively transformed from a wide-gap semiconductor into a metal via controlled lithium doping. We observe changes in the electron and phonon systems in 7-AGNRs upon lithium deposition using ARPES and UHV–Raman techniques. Electron transfer from lithium allows us to reach heavily doped regime (0.05 electrons/atom) and obtain the first direct proof of a combined band gap reduction by ≈0.3 eV and giant (supposed by a factor of four) effective mass renormalization in 1D system. These effects will be important for future graphene nanoelectronic devices utilizing the transport and optical properties of graphene nanoribbons. The combined investigation of the electron and phonon structures allowed us to explain the Raman shifts in electron-doped GNRs by the setting impact of the lattice relaxation and dynamic effects. The observed Raman intensity decrease upon doping is attributed to the changes in the quasiparticle dispersion and exciton binding energy. We propose GNRs as a unique platform for combined experimental and theoretical studies embracing many-body interactions. Our findings have relevance for the large 1D materials community and it lays the foundations for further studies of doped graphene nanoribbons.

Experimental Section

Experimental Details: 7-AGNRs were synthesized by surface polymerization of 10,10-dibromo-9,9-bianthryl (DBBA) molecules[13] on Au(111) and Au(788) surfaces. Au substrates were cleaned by three cycles of Ar+ sputtering (800 V) and subsequent annealing at 500 °C. The clean surface of Au(788) is shown in the Supporting Information. DBBA molecules were evaporated from a quartz crucible using a homebuilt evaporator with a thermocouple attached to the molecule reservoir. The deposition rate was controlled using a quartz microbalance. About 8 Å of precursor molecules (using the graphite density and *Z*-factor) were evaporated onto the Au surface which was kept at room temperature. Hereafter, a two-step polymerization reaction was performed: a 200 °C annealing step followed by a 400 °C annealing step, which induce debromination and cyclodehydrogenation reactions, respectively. The annealing was carried out using a computer controlled ramp that increased temperature over several hours. Lithium deposition (from 1 to 3 monolayers) was performed separately for ARPES, NEXAFS, and UHV Raman measurements using commercial SAES getters, calibrated with quartz microbalance. The maximum Li coverage was identical for all methods. The sample was kept at 80 K for ARPES measurements and at room temperature for other studies.

ARPES was carried out at the I3 beamline of the MAX IV synchrotron radiation facility (Lund, Sweden) using a Scienta R-4000 hemispherical electron analyser. The ARPES spectra were measured using photon energy of 32 eV in the second BZ of the GNRs and shifted back by application of the reciprocal lattice vector to the first BZ. The samples for ARPES measurements were synthesized and checked in the UHV Raman chamber and then transferred under UHV conditions into a special container which was filled then to a slight overpressure (1.1 bar) by high-purity Ar gas. Samples in UHV tight vacuum suitcases filled with an Ar were transported to the load-lock chamber of the ARPES beamline endstation and later gently annealed (at 200 °C) under UHV conditions. This method allowed us to achieve reproducible experimental results. For determination of the parabola maxima and the effective masses we performed a parabolic fit to the experimental energy distribution curve (EDC) maxima. The fits were performed within a region of sufficient signal/background ratio and hence have different wavevector limits. The physical origins for the wavevector dependence of the photoemission signal are the matrix elements and the overlap with Au states.

The STM data of clean Au(788) and 7-AGNRs/Au(788) are shown in the Supporting Information. STM measurements were performed using an Omicron LT-STM with the samples held at 4.5 K in UHV. A tungsten tip was used for topography and spectroscopic measurements. Prior to performing STS on the fully GNR covered Au(788), we prepared the tip on a clean Au(111) surface until we obtained pristine Au background spectra. This tip was then used for measurements on Au(788) and afterward checked again on clean Au(111) to ensure the tip did not change during measurements. Topographic images were acquired in constant current mode. d*I*/d*V* spectra were obtained using the lock-in technique where the tip bias was modulated by a 457 Hz, 10 mV (rms) sinusoidal voltage under open-feedback conditions. All STM images were processed with WSxM.[53]

UHV–Raman was performed in the back-scattering geometry using commercial Raman systems (Renishaw and OceanOptics) integrated in a homebuilt optical chamber where the exciting and Raman scattered light were coupled into the vacuum using a long-working distance microscope objective with an NA of ≈0.4. The laser power on the sample was kept below 1 mW. The analysis chamber of the UHV–Raman was attached to another chamber for sample preparation where the 7-AGNR synthesis, LEED characterization, and Li deposition were performed. Raman spectra were calibrated using Si peak at 520.5 cm^{-1} as well as oxygen peak at 1555 cm^{-1}.

XPS and NEXAFS experiments were performed at the German-Russian beamline (RGBL) of the HZB BESSY II synchrotron radiation facility (Berlin, Germany). XPS spectra were measured with photon energy of 320 eV and pass energy of 10 eV in the normal emission geometry. Samples were synthesized in the UHV Raman system and transferred to the synchrotron in the same manner as described for ARPES measurements. XPS data indicated no trace of oxygen as confirmed by the absence of an O1s peak (see survey spectrum in the Supporting Information). All XPS spectra were calibrated using the Au 4f7/2 core level at a binding energy 84.0 eV. NEXAFS data were obtained in total electron yield mode with an energy resolution of 50 meV close to the C K-edge.

Computational Details: Our first-principles calculations have been performed in the framework of the density functional theory[54] by using pseudopotentials obtained by the projector augmented wave method[55] and the Perdew–Burke–Ernzerhof exchange-correlation energy functional[56] as implemented in the Vienna ab initio simulation package code.[57,58] The ground-state adsorption geometry of Li on the $C_{14}H_4$ nanoribbon was obtained for an energy cutoff of 500 eV and by including the van der Waals interactions with the help of the nonlocal correlation energy functional vdW-DF2[59] together with the exchange energy functional developed by Hamada.[60]

Supporting Information

Supporting Information is available from the Wiley Online Library or from the author.

Acknowledgements

B.S., A.F., M.H., and A.G. acknowledge the ERC Grant No. 648589 "SUPER-2D," support from the DFG through the CRC1238 (project A1) and DFG project GR 3708/2-1. N.I.V. acknowledges the Russian Science Foundation (No. 14-13-00747). This research was supported by the U.S. Department of Energy (DOE), Office of Science, Basic Energy Sciences (BES), under Award No. DE-SC0010409 (design, synthesis, and characterization of molecular building blocks) and the Center for Energy Efficient Electronics Science NSF Award No. 0939514 (SPM imaging and spectroscopy). K.S. and A.P. acknowledge support from the Swedish Research Council and the ERC Grant No. 321319.

Received: November 11, 2016
Revised: December 23, 2016
Published online: March 10, 2017

[1] X. Li, X. Wang, L. Zhang, S. Lee, H. Dai, *Science* **2008**, *319*, 1229.
[2] F. Schwierz, *Nat. Nanotechnol.* **2010**, *5*, 487496.
[3] Z. Chen, Y.-M. Lin, M. J. Rooks, P. Avouris, *Physica E* **2007**, *40*, 228.
[4] X. Wang, Y. Ouyang, X. Li, H. Wang, J. Guo, H. Dai, *Phys. Rev. Lett.* **2008**, *100*, 206803.
[5] L. Liao, J. Bai, R. Cheng, Y.-C. Lin, S. Jiang, Y. Huang, X. Duan, *Nano Lett.* **2010**, *10*, 1917.
[6] K. Nakada, M. Fujita, G. Dresselhaus, M. S. Dresselhaus, *Phys. Rev. B* **1996**, *54*, 17954.
[7] L. Yang, L. C.-H. Park, Y.-W. Son, M. L. Cohen, S. G. Louie, *Phys. Rev. Lett.* **2007**, *99*, 186801.
[8] M. Y. Han, B. Ozyilmaz, Y. Zhang, P. Kim, *Phys. Rev. Lett.* **2007**, *98*, 206805.
[9] V. Barone, O. Hod, G. E. Scuseria, *Nano Lett.* **2006**, *6*, 2748.
[10] K. Wakabayashi, K.-I. Sasaki, T. Nakanishi, T. Enoki, *Sci. Technol. Adv. Mater.* **2010**, *11*, 054504.
[11] J. R. Sanchez-Valencia, T. Dienel, O. Gröning, I. Shorubalko, A. Mueller, M. Jansen, K. Amsharov, P. Ruffieux, R. Fasel, *Nature* **2014**, *512*, 61.
[12] L. Grill, M. Dyer, L. Lafferentz, M. Persson, M. V. Peters, S. Hecht, *Nat. Nanotechnol.* **2007**, *2*, 687.
[13] J. Cai, P. Ruffieux, R. Jaafar, M. Bieri, T. Braun, S. Blankenburg, M. Muoth, A. P. Seitsonen, M. Saleh, X. Feng, K. Müllen, R. Fasel, *Nature* **2010**, *466*, 470.
[14] Y.-C. Chen, D. G. de Oteyza, Z. Pedramrazi, C. Chen, F. R. Fischer, M. F. Crommie, *ACS Nano* **2013**, *7*, 6123.
[15] Y.-C. Chen, T. Cao, C. Chen, Z. Pedramrazi, D. Haberer, D. G. de Oteyza, F. R. Fischer, M. Crommie, *Nat. Nanotechnol.* **2015**, *10*, 156.
[16] R. R. Cloke, T. Marangoni, G. D. Nguyen, T. Joshi, D. J. Rizzo, C. Bronner, T. Cao, S. G. Louie, M. F. Crommie, F. R. Fischer, *J. Am. Chem. Soc.* **2015**, *137*, 8872.
[17] S. Kawai, S. Saito, S. Osumi, S. Yamaguchi, A. S. Foster, P. Spijker, E. Meyer, *Nat. Commun.* **2015**, *6*, 8098.
[18] A. Kimouche, M. M. Ervasti, R. Drost, S. Halonen, A. Harju, P. M. Joensuu, J. Sainio, P. Liljeroth, *Nat. Commun.* **2015**, *6*, 10177.
[19] P. Ruffieux, S. Wang, B. Yang, C. Sánchez-Sánchez, J. Liu, T. Dienel, L. Talirz, P. Shinde, C. A. Pignedoli, D. Passerone, T. Dumsla, X. Feng, K. Müullen, R. Fasel, *Nature* **2016**, *531*, 489492.
[20] L. Talirz, P. Ruffieux, R. Fasel, *Adv. Mater.* **2016**, *28*, 6222.
[21] S. Das Sarma, D. W. Wang, *Phys. Rev. Lett.* **2000**, *84*, 2010.
[22] C. D. Spataru, F. Léonard, *Phys. Rev. Lett.* **2010**, *104*, 177402.
[23] S. Gao, Y. Liang, C. D. Spataru, L. Yang, *Nano Lett.* **2016**, *16*, 5568.
[24] D. Prezzi, D. Varsano, A. Ruini, A. Marini, E. Molinari, *Phys. Rev. B* **2008**, *77*, 041404.
[25] D. Prezzi, D. Varsano, A. Ruini, E. Molinari, *Phys. Rev. B* **2011**, *84*, 041401.
[26] P. Ruffieux, J. Cai, N. C. Plumb, L. Patthey, D. Prezzi, A. Ferretti, E. Molinari, X. Feng, K. Müllen, C. A. Pignedoli, R. Fasel, *ACS Nano* **2012**, *6*, 6930.
[27] J. U. Lee, *Phys. Rev. B* **2007**, *75*, 075409.
[28] M. Steiner, M. Freitag, V. Perebeinos, A. Naumov, J. P. Small, A. A. Bol, P. Avouris, *Nano Lett.* **2009**, *9*, 3477.
[29] H. Hartleb, F. Späth, T. Hertel, *ACS Nano* **2015**, *9*, 10461.
[30] Y. Miyauchi, Z. Zhang, M. Takekoshi, Y. Tomio, H. Suzuura, V. Perebeinos, V. V. Deshpande, C. Lu, S. Berciaud, P. Kim, J. Hone, T. F. Heinz, *Phys. Rev. B* **2015**, *92*, 205407.
[31] S. Linden, D. Zhong, A. Timmer, N. Aghdassi, J. H. Franke, H. Zhang, X. Feng, K. Müllen, H. Fuchs, L. Chi, H. Zacharias, *Phys. Rev. Lett.* **2012**, *108*, 216801.
[32] M. Koch, F. Ample, C. Joachim, L. Grill, *Nat. Nanotechnol.* **2012**, *7*, 713.
[33] H. Söde, L. Talirz, O. Gröning, C. A. Pignedoli, R. Berger, X. Feng, K. Müllen, R. Fasel, P. Ruffieux, *Phys. Rev. B* **2015**, *91*, 045429.
[34] G. Vasseur, Y. Fagot-Revurat, M. Sicot, B. Kierren, L. Moreau, D. Malterre, L. Gardenas, G. Galeotti, J. Lipton-Duffin, F. Rosei, M. Di Giovannantonio, G. Contini, P. Le Fevre, F. Bertran, L. Liang, V. Meunier, D. F. Perepichka, *Nat. Commun.* **2016**, *7*, 10235.
[35] M. M. Ugeda, A. J. Bradley, S.-F. Shi, F. H. da Jornada, Y. Zhang, D. Y. Qiu, W. Ruan, S.-K. Mo, Z. Hussain, Z.-X. Shen, F. Wang, S. G. Louie, M. F. Crommie, *Nat. Mater.* **2014**, *13*, 1091.
[36] M. Ezawa, *Phys. Rev. B* **2006**, *73*, 045432.
[37] Y.-W. Son, M. L. Cohen, S. G. Louie, *Phys. Rev. Lett.* **2006**, *97*, 216803.
[38] S. Wang, L. Talirz, C. A. Pignedoli, X. Feng, R. F. Klaus Müllen, P. Ruffieux, *Nat. Commun.* **2016**, *7*, 11507.
[39] K. A. Simonov, N. A. Vinogradov, A. S. Vinogradov, A. V. Generalov, E. M. Zagrebina, N. Mårtensson, A. A. Cafolla, T. Carpy, J. P. Cunniffe, A. B. Preobrajenski, *J. Phys. Chem. C* **2014**, *118*, 12532.
[40] N. I. Verbitskiy, A. V. Fedorov, C. Tresca, G. Profeta, L. Petaccia, B. V. Senkovskiy, D. Y. Usachov, D. V. Vyalikh, L. V. Yashina, A. A. Eliseev, T. Pichler, A. Grüneis, *2D Mater.* **2016**, *3*, 045003.
[41] J. W. Negele, H. Orland, *Quantum Many-Particle Systems*, Advanced Books Classics, Westview, Boulder, CO **1998**.
[42] A. V. Fedorov, N. I. Verbitskiy, D. Haberer, C. Struzzi, L. Petaccia, D. Usachov, O. Y. Vilkov, D. V. Vyalikh, J. Fink, M. Knupfer, B. Büchner, A. Grüneis, *Nat. Commun.* **2014**, *5*, 4257.
[43] P. E. Trevisanutto, C. Giorgetti, L. Reining, M. Ladisa, V. Olevano, *Phys. Rev. Lett.* **2008**, *101*, 226405.
[44] R. Denk, M. Hohage, P. Zeppenfeld, J. Cai, C. A. Pignedoli, H. Söde, R. Fasel, X. Feng, K. Müllen, S. Wang, D. Prezzi, A. Ferretti, A. Ruini, E. Molinari, P. Ruffieux, *Nat. Commun.* **2014**, *5*, 4253.

[45] H. Kuzmany, W. Plank, M. Hulman, C. Kramberger, A. Grüneis, T. Pichler, H. Peterlik, H. Kataura, Y. Achiba, *Eur. Phys. J. B* **2001**, *22*, 307.
[46] A. Das, S. Pisana, B. Chakraborty, S. Piscanec, S. K. Saha, U. V. Waghmare, K. S. Novoselov, H. R. Krishnamurthy, A. K. Geim, A. C. Ferrari, A. K. Sood, *Nat. Nanotechnol.* **2008**, *3*, 210.
[47] J. Yan, Y. Zhang, P. Kim, A. Pinczuk, *Phys. Rev. Lett.* **2007**, *98*, 166802.
[48] A. Das, A. K. Sood, *Phys. Rev. B* **2009**, *79*, 235429.
[49] B. Chakraborty, A. Bera, D. V. S. Muthu, S. Bhowmick, U. V. Waghmare, A. K. Sood, *Phys. Rev. B* **2012**, *85*, 161403.
[50] S. Pisana, M. Lazzeri, C. Casiraghi, K. Novoselov, A. Geim, A. Ferrari, F. Mauri, *Nat. Mater.* **2007**, *6*, 198.
[51] N. Caudal, A. M. Saitta, M. Lazzeri, F. Mauri, *Phys. Rev. B* **2007**, *75*, 115423.
[52] J. C. Tsang, M. Freitag, V. Perebeinos, J. Liu, P. Avouris, *Nat. Nanotechnol.* **2007**, *2*, 725.
[53] I. Horcas, R. Fernandez, J. Gomez-Rodriguez, J. Colchero, J. Gomez-Herrero, A. Baro, *Rev. Sci. Instrum.* **2007**, *78*, 013705.
[54] W. Kohn, L. J. Sham, *Phys. Rev.* **1965**, *140*, A1133.
[55] P. E. Blöchl, *Phys. Rev. B* **1994**, *50*, 17953.
[56] J. Perdew, K. Burke, M. Ernzerhof, *Phys. Rev. Lett.* **1996**, *77*, 3865.
[57] G. Kresse, J. Hafner, *Phys. Rev. B* **1993**, *47*, 558.
[58] G. Kresse, J. Furthmüller, *Phys. Rev. B* **1996**, *54*, 11169.
[59] K. Lee, E. D. Murray, L. Kong, B. I. Lundqvist, D. C. Langreth, *Phys. Rev. B* **2010**, *82*, 081101.
[60] I. Hamada, *Phys. Rev. B* **2014**, *89*, 121103.